# Nanoscale

Accepted Manuscript


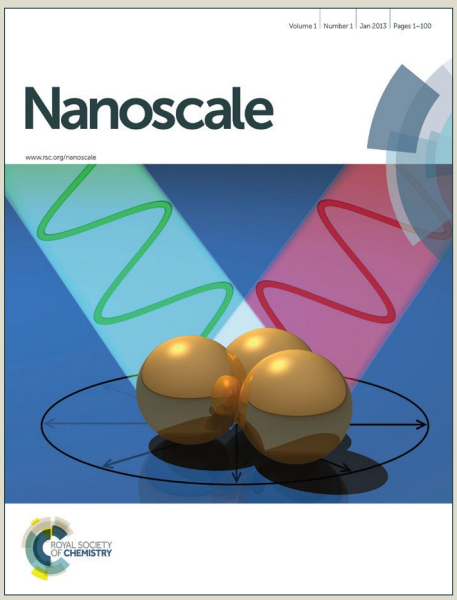





ROYAL SOCIETY OF CHEMISTRY

www.rsc.org/nanoscale

Nanoscale

PAPER

# Doping-free bandgap tuning in one-dimensional Magnéli-phase nanorods of $Mo_4O_{11}$†

Received 00th January 20xx,
Accepted 00th January 20xx

DOI: 10.1039/x0xx00000x

www.rsc.org/

Duy Van Pham,[a] Ranjit A. Patil, **[a], Jin-Han Lin,[b] Chien-Chih Lai,[a] Yung Liou,[b] and Yuan-Ron Ma, *[a]

We synthesized one-dimensional (1D) Magnéli-phase nanorods of $Mo_4O_{11}$ using the hot filament metal-oxide vapor deposition technique. The 1D Magnéli-phase $Mo_4O_{11}$ nanorods synthesized at 1000, 1050, 1100, 1150, and 1200 ºC contain varying combinations of two orthorhombic (*α*) and monoclinic (*η*) phases, and various mixtures of $Mo^{4+}$, $Mo^{5+}$ and $Mo^{6+}$ cations, while those synthesized at a higher temperature look bluer. The shifts of the transmittance maximum and absorbance minimum of the 1D Magnéli-phase $Mo_4O_{11}$ nanorods are inversely and linearly proportional to the elevated temperature, verifying that the bandgaps (Eg) are inversely proportional to the elevated temperature. The bandgap ($E_g$) of the 1D Magnéli-phase $Mo_4O_{11}$ nanorods can be tuned simply by controlling the synthesis temperature without doping with other materials, giving the 1D Magnéli-phase $Mo_4O_{11}$ nanorods good potential for use in optoelectronic nanodevices and bandgap engineering.

## Introduction

A variety of methods[1-3] have been used to dope other elements into host materials. Doping can strongly affect the properties of these materials[4-6] and it is crucial to tune or tailor the bandgaps for materials to be used in optical and optoelectronic devices. Although current doping methods offer good control for bandgap tuning, the intrinsic properties of the host materials are lost. The search for a method for doping-free bandgap tuning for materials to be used in optoelectronics and optical devices is promising.[7,8] Molybdenum oxides can play important roles in bandgap tuning, because they possess many stable and metastable crystal phases[9] with varying valences. The various stable and metastable crystal phases can be simply controlled with many factors, such as high pressure,[10] substrate temperature,[11,12] and even oxygen atmosphere,[13] which can be used to change or tune the bandgaps. In addition, molybdenum oxides have versatile optical and electronic properties, which give them potential for use in practical devices such as field emission,[14] electrochromic[15] and photochromic windows,[16] Li-ion batteries,[17-19] field effect transistors (FETs),[20] hydro-deoxygenation (HDO),[21] photocatalysts,[22,23] and gas sensors for ethanol,[13,24,25] $H_2$,[25] $NO_2$,[26] and $NH_3$.[26,27] As mentioned above, molybdenum oxides have many stable and metastable crystal phases with varying valences, so they can form in varying stoichiometric forms, for example, $MoO_2$,[28] h-$MoO_3$,[22,29] α-$MoO_3$,[22-24] *β*-$MoO_3$,[17] Magnéli phases like $Mo_4O_{11}$,[30-33] and the non-stoichiometric $MoO_x$.[34]

In this work, we synthesized large-area arrays of one-dimensional (1D) Magnéli phase nanorods of $Mo_4O_{11}$ on conducting indium-tin-oxide (ITO) thin films coated on glass substrates using the hot-filament metal-oxide vapour deposition (HFMOVD) technique. The Magnéli phase of $Mo_4O_{11}$ contains orthorhombic (*α*) and monoclinic (*η*) crystals[30-33] and a mixture of $Mo^{4+}$, $Mo^{5+}$ and $Mo^{6+}$ cations. The structural morphology and size distribution of the 1D Magnéli-phase $Mo_4O_{11}$ nanorods were examined through field-emission scanning electron microscopy (FESEM) and transmission electron microscopy (TEM). The crystalline structures of the 1D Magnéli-phase $Mo_4O_{11}$ nanorods were substantiated by x-ray diffractometry (XRD), selected-area electron diffractometry (SAED), and Raman spectroscopy. The electronic structures, chemical properties and stoichiometry of the 1D Magnéli-phase $Mo_4O_{11}$ nanorods were verified by x-ray photoemission spectroscopy (XPS). Optical spectroscopy is a well-developed tool for the inspection of semiconductor materials for determination of the bandgaps. The bandgaps of 1D Magnéli-phase $Mo_4O_{11}$ nanorods synthesized at varying synthesis temperatures can be acquired through absorbance and transmittance measurements. The bandgap decreases linearly with the elevation of temperature, meaning that the bandgaps of the 1D Magnéli-phase $Mo_4O_{11}$ nanorods can be tuned or tailored without doping with other materials. Obviously, the bandgap tuning occurs due to varying combinations of two orthorhombic (*α*) and monoclinic (*η*) phases and various mixtures of the $Mo^{4+}$, $Mo^{5+}$ and $Mo^{6+}$ cations. The bandgap

[a] Department of Physics, National Dong Hwa University, Hualien 97401, Taiwan.
[b] Institute of Physics, Academia Sinica, Taipei 11529, Taiwan
* Corresponding author, ronma@mail.ndhu.edu.tw.
** Co-corresponding author, ranajit27@gmail.com

† Electronic Supplementary Information (ESI) available: statistical distribution of the widths of the nanorods, crystalline phase quantification, raman shifts of the raman scattering peaks. See DOI: 10.1039/x0xx00000x

results strongly confirm the viability of the 1D Magnéli-phase $Mo_4O_{11}$ nanorods as potential candidate materials for the fabrication of optoelectronic nanodevices in bandgap engineering.

## Experimental

### Synthesis of 1D $Mo_4O_{11}$ nanorods

Large-area arrays of the 1D Magnéli phase nanorods of $Mo_4O_{11}$ were synthesized on transparent and conducting ITO thin films (~8 Ω·cm) coated on glass substrates using the HFMOVD technique. The HFMOVD technique has been used to synthesize a variety of nanostructures with different morphologies and crystalline traits.[35-38] A clean molybdenum (Mo) wire (99.9 % pure) with a diameter of ~1 mm was fixed to two supporting copper (Cu) electrodes in a vacuum chamber. When the pressure of the chamber was pumped down to $1\times10^{-2}$ Torr, pure argon (Ar) gas was input and then maintained at a pressure of ~10 Torr. A Mo wire was heated to 1000, 1050, 1100, 1150, and 1200 $^{o}$C, for 30 min to generate hot Mo vapor. The hot Mo vapor encountered and reacted with the residual oxygen to form $MoO_x$ vapor. Upon encountering the ITO/glass substrate which had been placed on the graphite disc holder (~3 mm above the Mo-wires) the $MoO_x$ condensed to form 1D Magnéli-phase $Mo_4O_{11}$ nanorods.

### Characterization of 1D $Mo_4O_{11}$ nanorods

The surface morphology of the 1D Magnéli-phase $Mo_4O_{11}$ nanorods thus produced was characterized by a field emission scanning electron microscope (FESEM, JEOL JSM-6500F). The crystalline structure of the 1D Magnéli-phase $Mo_4O_{11}$ nanorods was confirmed using an x-ray diffractometer (Philips X'Pert PRO) with Cu Kα radiation (λ=1.541 Å) and a Raman spectrometer (Horiba Scientific, Triax 550) with 532 nm incident photons from a diode-pump solid state laser. Structural analysis of the 1D Magnéli-phase $Mo_4O_{11}$ nanorods was also carried out using a transmission electron microscope (TEM, JEOL JEM-2100) with a selected-area electron diffractometer (SAED) at an accelerating voltage of 200 kV. The SAED patterns were simulated with the crystallographic software (CaRIne version 3.1). The elemental and local structural information of the 1D Magnéli-phase $Mo_4O_{11}$ nanorods was analyzed using an x-ray photoelectron spectrometer (XPS, Thermo Scientific Inc. K-alpha) with a microfocus monochromated Al K*α* x-ray. The transmittance and absorbance of the 1D Magnéli-phase $Mo_4O_{11}$ nanorods were acquired in the range from ultraviolet (UV) to infrared (IR) light using an optical spectrometer (Spectra Academy, SV2100).

## Results and discussion

The FESEM images in Fig. 1 show the surface morphology of the 1D Magnéli-phase $Mo_4O_{11}$ nanorods. The top views of the large-area arrays of 1D Magnéli-phase $Mo_4O_{11}$ nanorods produced at various temperatures of 1000, 1050, 1100, 1150, and 1200 $^{o}$C, are shown in

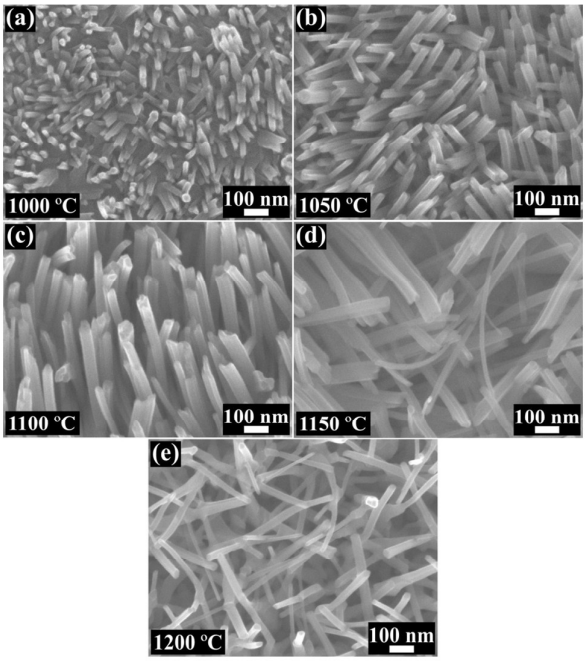


**Fig. 1** FESEM images showing the surface morphology of the 1D Magnéli-phase $Mo_4O_{11}$ nanorods synthesized at various temperatures of (a) 1000 °C (b) 1050 °C (c) 1100 °C (d) 1150 °C and (e) 1200 ºC. The nanorods are all similar in appearance and possess clear textural boundaries. The statistical histograms (see ESI, Fig. S1) display the width distributions of the 1D Magnéli-phase $Mo_4O_{11}$ nanorods.

Fig. 1(a)-1(e). All the 1D Magnéli-phase $Mo_4O_{11}$ nanorods look similar and possess clear textural boundaries. The width distribution of the 1D Magnéli-phase $Mo_4O_{11}$ nanorods can be statistically gathered and fitted by the lognormal distribution function.[35] The statistical histograms (see ESI, Fig. S1) display the width distributions of the 1D Magnéli-phase $Mo_4O_{11}$ nanorods. The widths of a large number of the 1D Magnéli-phase $Mo_4O_{11}$ nanorods fall into the range of ~20-60 nm. The 1D Magnéli-phase $Mo_4O_{11}$ nanorods are uniformly distributed on the ITO/glass substrates.

The FESEM images in Fig. 2(a)-2(e) show the side views of the large-area arrays of the 1D Magnéli-phase $Mo_4O_{11}$ nanorods synthesized at the temperatures of 1000, 1050, 1100, 1150, and 1200 $^{o}$C, respectively. It can be seen that the 1D Magnéli-phase $Mo_4O_{11}$ nanorods stand vertically on the ITO/glass substrates. Also, there is a $MoO_x$ buffer layer between the 1D nanorods and the ITO thin film for each array. The graph in Fig. 2(f) shows the average length of the 1D $Mo_4O_{11}$ nanorods and the thickness of the $MoO_x$ buffer layer *versus* temperature. The average length of the 1D $Mo_4O_{11}$ nanorods is linearly proportional to temperature elevation, while the thickness of the $MoO_x$ buffer layer is inversely proportional to elevated temperature. The two linear fitting results confirm that the lengths of the 1D $Mo_4O_{11}$ nanorods grow at the expense of the thickness of the $MoO_x$ buffer layers. The average lengths of the 1D Magnéli-phase $Mo_4O_{11}$ nanorods and the thickness of the $MoO_x$ buffer layers can be simply obtained and are shown in Table S1 (see ESI). Note that the 1D $Mo_4O_{11}$ nanorods and the $MoO_x$ buffer layer cannot be produced at temperatures below

1000 ºC or above 1200 ºC. In fact, $MoO_x$ microstructures or bulk material appear at temperatures above 1200 ºC.

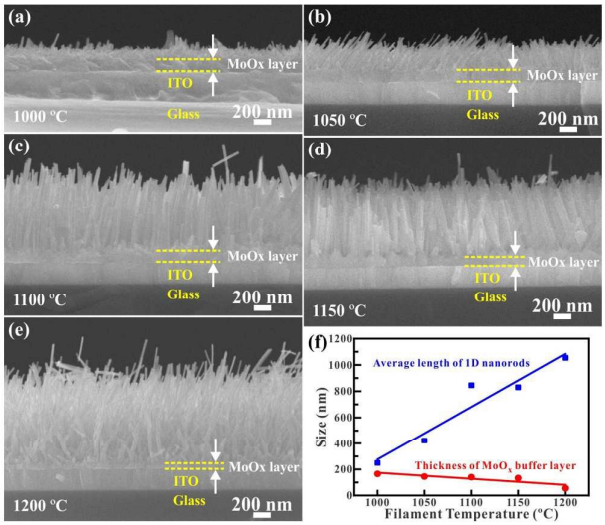


**Fig. 2** FESEM images showing side views of the large-area arrays of 1D Magnéli-phase $Mo_4O_{11}$ nanorods synthesized at the temperatures of 1000, 1050, 1100, 1150, and 1200 °C. (f) The graph displays the average length of the 1D $Mo_4O_{11}$ nanorods and the thickness of the $MoO_x$ buffer layer *versus* temperature. The average length of the 1D $Mo_4O_{11}$ nanorods and the thickness of the $MoO_x$ buffer layer are linearly and inversely proportional to elevated temperature.

XRD patterns are the fingerprints of crystals, and can help to distinguish between various crystalline structures in complicated crystals. Fig. 3 shows the six XRD spectra for the ITO substrate and the 1D Magnéli-phase $Mo_4O_{11}$ nanorods synthesized at the temperatures of 1000, 1050, 1100, 1150, and 1200 °C, respectively. The XRD patterns indicate the presence of $Mo_4O_{11}$ and ITO phases. All the XRD spectra, except for the ITO substrate, as shown in Fig. 3, have very similar patterns, indicating that the 1D Magnéli-phase $Mo_4O_{11}$ nanorods synthesized at varying temperatures consist of the same or similar crystalline phases. In fact, the diffraction peaks (indicated by $\alpha$ or/and $\eta$) reveal that the 1D Magnéli-phase $Mo_4O_{11}$ nanorods contain two crystals together, which are the orthorhombic ($\alpha$) phase in the space group *Pna*21 with lattice constants $a$=2.44 nm, $b$=0.67 nm, $c$=0.54 nm and $\alpha$=$\beta$=$\gamma$=90º (ICSD 654112), and the monoclinic ($\eta$) phase in the space group *P*121/*c*1 with $a$=0.67 nm, $b$=0.54 nm, $c$=2.45 nm and $\alpha$=$\gamma$=90º, $\beta$=94.3º (ICSD 82363), respectively. Note that the ITO thin film is a cubic crystal allocated to the space group *Ia*3 with lattice constants $a$=$b$=$c$=1.011 nm and $\alpha$=$\beta$=$\gamma$=90º (ICSD 50847). The statistics for the intensities of the diffraction peaks imply that the 1D Magnéli-phase $Mo_4O_{11}$ nanorods comprise various composition percentages (see ESI, Table S2) of the orthorhombic ($\alpha$) and monoclinic ($\eta$) phases at varying temperatures. At a temperature of 1000 °C, the orthorhombic ($\alpha$) and monoclinic ($\eta$) phases are in the minority and majority, respectively, in the 1D Magnéli-phase $Mo_4O_{11}$ nanorods. In contrast, the orthorhombic ($\alpha$) and monoclinic ($\eta$) phases become the majority and minority, respectively, in the 1D Magnéli-phase $Mo_4O_{11}$ nanorods fabricated at temperatures between 1050 and 1150 °C. However, the orthorhombic ($\alpha$) and monoclinic ($\eta$) phases are equivalent to each other at a temperature of 1200 °C. Clearly,

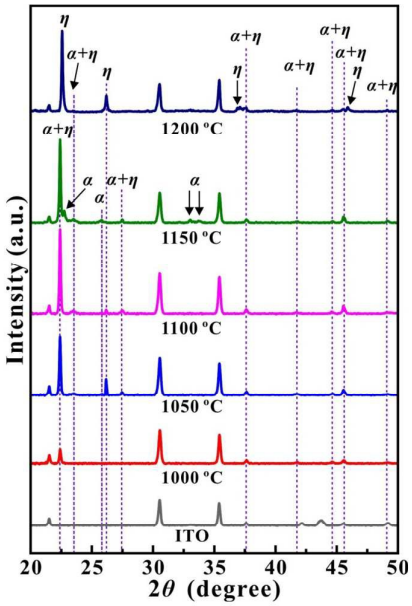


**Fig. 3** XRD spectra of the ITO substrate and the 1D Magnéli-phase $Mo_4O_{11}$ nanorods synthesized at the temperatures of 1000, 1050, 1100, 1150, and 1200 °C. The 1D Magnéli-phase $Mo_4O_{11}$ nanorods comprise various composition percentages (see ESI, Table S2) of the two orthorhombic ($\alpha$) and monoclinic ($\eta$) phases at varying temperatures.

the statistical results indicate the composition ratio of the orthorhombic ($\alpha$) phase to the monoclinic ($\eta$) phase to be strongly dependent on the temperature.

TEM is a powerful tool for examining the crystalline structure of a 1D Magnéli-phase $Mo_4O_{11}$ nanorod. Fig. 4 shows the TEM images and selected area electron diffraction (SAED) pattern of a single 1D Magnéli-phase $Mo_4O_{11}$ nanorod, and the simulated electron diffraction patterns. The TEM image in Fig. 4(a) shows a single 1D Magnéli-phase $Mo_4O_{11}$ nanorod about ~50 nm wide, and the high-magnification TEM in the inset to Fig. 4(a) displays the end of the nanorod. The single 1D Magnéli-phase $Mo_4O_{11}$ nanorod has a uniform width along its whole length, and the growth direction, indicated by an arrow, may be along the [002] direction for the orthorhombic ($\alpha$) phase or the [020] direction for the monoclinic ($\eta$) phase. This is because the single Magnéli-phase $Mo_4O_{11}$ nanorod contains both orthorhombic ($\alpha$) and monoclinic ($\eta$) phases, as mentioned above in the XRD results. The high-magnification TEM image in Fig. 4(b) shows that the visible parallel lattice fringes of the single 1D Magnéli-phase $Mo_4O_{11}$ nanorod are perpendicular to its growth axis. The $d$ spacing between two adjacent parallel lattice fringes is 0.32 nm, which corresponds to the $\alpha$(220) and $\eta$(202) planes in the orthorhombic and monoclinic phases of $Mo_4O_{11}$, respectively. The corresponding SAED pattern is shown in the inset to Fig. 4(b). The SAED pattern appears to show two phases of overlapping, because the reflections in the SAED pattern consist not only of diffraction spots but also diffraction lines. The complicated spots and lines may be caused by a mixture phase of the orthorhombic and monoclinic crystals in a single 1D Magnéli-phase

$Mo_4O_{11}$ nanorod. Based on the XRD results, the electron diffraction patterns for the two orthorhombic ($\alpha$) and monoclinic ($\eta$) phases with the zone [100] and [001] axes, respectively, can be simulated. are not clearly understood, and the structural properties need to be further explored. However, according to Ref. 34, there are many characteristic Raman bands (see ESI, Table S4), which reveal some

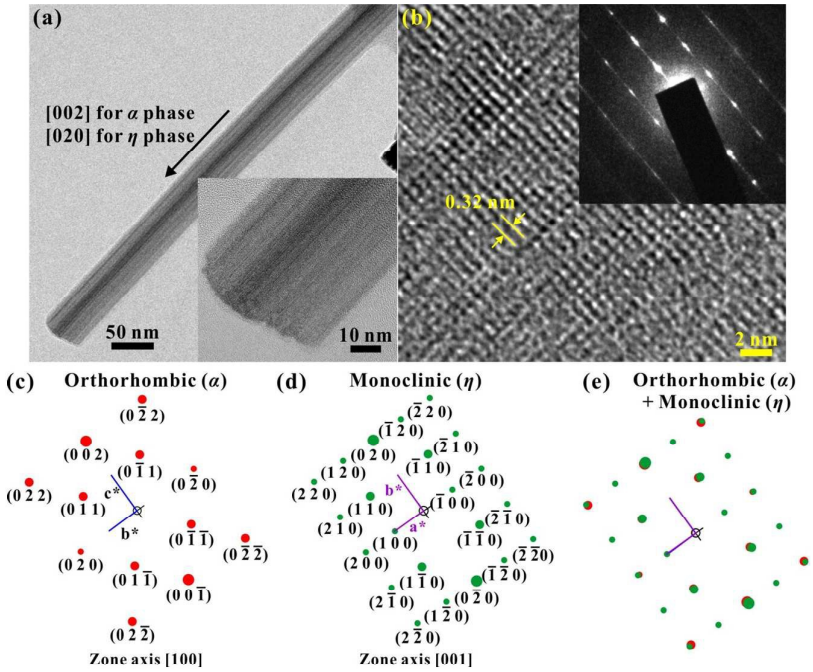


**Fig. 4** (a) TEM images showing a single 1D Magnéli-phase $Mo_4O_{11}$ nanorod synthesized at a temperature of 1150 ºC. The inset displays one of two ends, and the growth direction, indicated by an arrow, which may be along the [220] direction for the orthorhombic ($\alpha$) phase or the [202] direction for the monoclinic ($\eta$) phase. (b) The high-magnification TEM image shows that *d* spacing between two adjacent parallel lattice fringes is 0.32 nm, which corresponds to the $\alpha$(220) or $\eta$(202) planes in orthorhombic and monoclinic phases of $Mo_4O_{11}$, respectively. The inset illustrates the corresponding SAED pattern consisting not only of diffraction spots but also diffraction lines. (c) and (d) Two schematic diagrams display the two simulated electron diffraction patterns for the two orthorhombic ($\alpha$) and monoclinic ($\eta$) phases, respectively. (e) When the two simulated electron patterns are overlapped, all the reflections of the orthorhombic ($\alpha$) phase are exactly superposed at those of the monoclinic ($\eta$) phases.

The two simulated electron diffraction patterns are shown in Figs. 4(c) and 4(d), and all the reflections are assigned to the indications of the lattice planes. When the two simulated electron patterns are overlapped, the reflections of the orthorhombic ($\alpha$) phase are exactly superposed over those of the monoclinic ($\eta$) phases, as shown in Fig. 4(e). The superposed electron diffraction patterns verify that the SAED pattern in the inset to Fig. 4(b) possesses two overlapping phases, and confirms that a single 1D Magnéli-phase $Mo_4O_{11}$ nanorod consists of the two orthorhombic ($\alpha$) and monoclinic ($\eta$) phases.

The Raman spectra in Fig. 5 show the Raman scattering results for the structural properties of the 1D Magnéli-phase $Mo_4O_{11}$ nanorods on ITO substrates. All the observed Raman bands of the 1D Magnéli-phase $Mo_4O_{11}$ nanorods synthesized at the temperatures of 1000, 1050, 1100, 1150, and 1200 $^{o}$C are specified in Table S3 (see ESI). The five Raman spectra in Fig. 5 obviously differ from each other, indicating that the 1D Magnéli-phase $Mo_4O_{11}$ nanorods, synthesized at the temperatures of 1000, 1050, 1100, 1150, and 1200 $^{o}$C, have various structural properties. There have been very few studies.[30,34,39,40] reporting the Raman scattering of $Mo_4O_{11}$ crystals, and the results are not in agreement with each other. There is also disagreement in the five Raman spectra taken of the 1D Magnéli-phase $Mo_4O_{11}$ nanorods shown in Fig. 5. Hence, the molecular vibrations of the 1D Magnéli-phase $Mo_4O_{11}$ nanorods

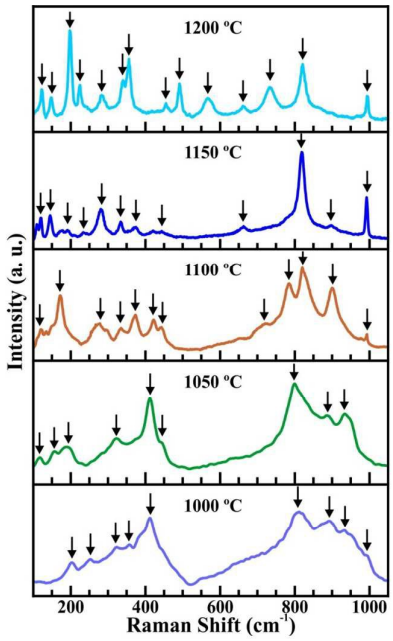


**Fig. 5** Raman spectra showing Raman scattering results for the structural properties of the 1D Magnéli-phase $Mo_4O_{11}$ nanorods on ITO substrates. All observed Raman bands (indicated by arrows) of the 1D Magnéli-phase $Mo_4O_{11}$ nanorods synthesized at the temperatures of 1000, 1050, 1100, 1150, and 1200 $^{o}$C are specified in Table S3 (see ESI).

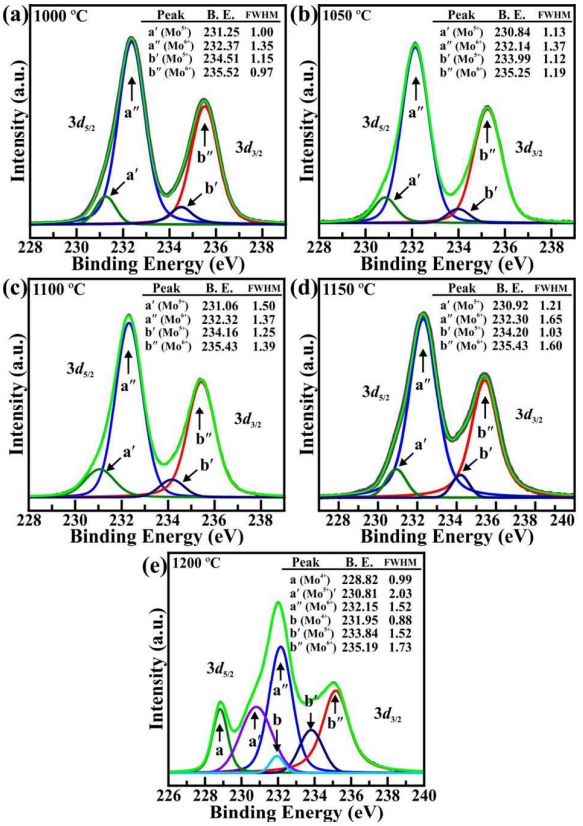


**Fig. 6** XPS spectra of the 1D Magnéli-phase $Mo_4O_{11}$ nanorods synthesized at temperatures of 1000, 1050, 1100, 1150, and 1200 ºC, respectively. (a)-(d) All the XPS spectra show the same $Mo^{5+}$ $3d_{5/2}$, $Mo^{5+}$ $3d_{3/2}$, $Mo^{6+}$ $3d_{5/2}$, and $Mo^{6+}$ $3d_{3/2}$ peaks. (e) There are two more $Mo^{4+}$ $3d_{5/2}$ and $Mo^{4+}$ $3d_{3/2}$ peaks. All the XPS spectra were decomposed via Voigt function fitting following a Shirley background. Note that the peaks for the $Mo^{4+}$ $3d_{5/2}$, $Mo^{5+}$ $3d_{5/2}$, $Mo^{6+}$ $3d_{5/2}$, $Mo^{4+}$ $3d_{3/2}$, $Mo^{5+}$ $3d_{3/2}$, and $Mo^{6+}$ $3d_{3/2}$ core levels are labeled **a**, **a′**, **a"**, **b**, **b′**, and **b"**, respectively.

clues for the molecular vibrations of 1D Magnéli-phase $Mo_4O_{11}$ nanorods. For example, the Raman bands at small, medium, and large Raman shifts represent $MoO_4$-chain translations, O-M-O (or O=M=O) scissors (or wagging, bending, twisting), and M=O (or O-M-O) stretches, respectively. The varying phonons give the 1D Magnéli-phase $Mo_4O_{11}$ nanorods potential for use in phononics.[41-44]

XPS was utilized to perform quantitative analysis of the electronic structures and chemical composition of the 1D Magnéli-phase $Mo_4O_{11}$ nanorods. Fig. 6 show a series of XPS spectra for 1D Magnéli-phase $Mo_4O_{11}$ nanorods synthesized at temperatures of 1000, 1050, 1100, 1150, and 1200 ºC. All the XPS spectra in Figs. 6(a)-6(d) show the same $Mo^{5+}$ $3d_{5/2}$, $Mo^{5+}$ $3d_{3/2}$, $Mo^{6+}$ $3d_{5/2}$, and $Mo^{6+}$ $3d_{3/2}$ peaks, while Fig. 6(e) displays not only the $Mo^{5+}$ $3d_{5/2}$, $Mo^{5+}$ $3d_{3/2}$, $Mo^{6+}$ $3d_{5/2}$, and $Mo^{6+}$ $3d_{3/2}$ peaks, but also the $Mo^{4+}$ $3d_{5/2}$ and $Mo^{4+}$ $3d_{3/2}$ peaks. To precisely determine the features of the double or multiple peaks of the Mo $3d_{5/2}$ and Mo $3d_{3/2}$ core levels, all the XPS spectra were decomposed via Voigt function fitting following a Shirley background. Note that the peaks for the $Mo^{4+}$ $3d_{5/2}$, $Mo^{5+}$ $3d_{5/2}$, $Mo^{6+}$ $3d_{5/2}$, $Mo^{4+}$ $3d_{3/2}$, $Mo^{5+}$ $3d_{3/2}$, and $Mo^{6+}$ $3d_{3/2}$ core levels are labeled **a**, **a′**, **a″**, **b**, **b′**, and **b″**, respectively. It is clear that the 1D Magnéli-phase $Mo_4O_{11}$ nanorods synthesized at

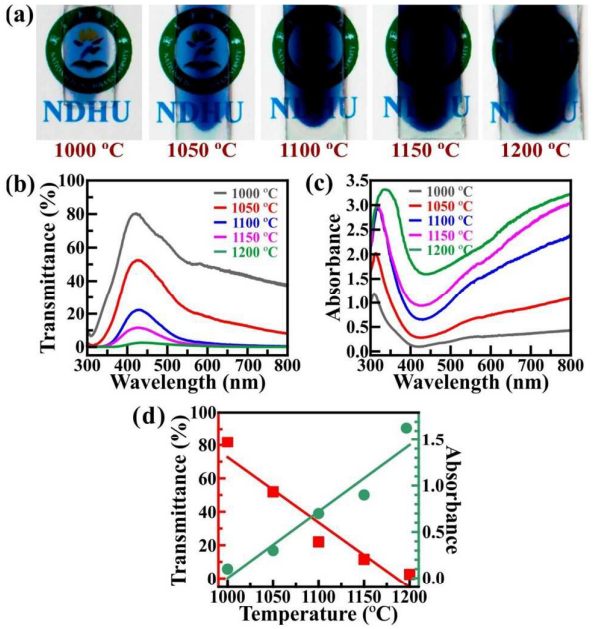


**Fig. 7** (a) Photographs showing the 1D Magnéli-phase $Mo_4O_{11}$ nanorods grown on the ITO/glass substrates at the temperatures of 1000, 1050, 1100, 1150, and 1200 ºC. The nanorods synthesized at higher temperature are bluer. (b) The transmittance and (c) absorbance spectra of the 1D Magnéli-phase $Mo_4O_{11}$ nanorods synthesized at various temperatures. (d) The graph shows that the transmittance is inversely proportional to the temperature, but the absorbance is linearly proportional to the temperature.

temperatures of 1000, 1050, 1100, and 1150 ºC contain two $Mo^{5+}$ and $Mo^{6+}$ cations. The $Mo^{5+}$ and $Mo^{6+}$ cations are around 9-14 % and 86-91 %, respectively. However, the 1D Magnéli-phase $Mo_4O_{11}$ nanorods synthesized at 1200 ºC comprise three $Mo^{4+}$, $Mo^{5+}$ and $Mo^{6+}$ cations. The $Mo^{4+}$, $Mo^{5+}$ and $Mo^{6+}$ cations are approximately 13, 29, and 58 %, respectively. Therefore, the XPS results verify that 1D Magnéli-phase $Mo_4O_{11}$ nanorods synthesized at various temperatures have varying mixtures of $Mo^{4+}$, $Mo^{5+}$ and $Mo^{6+}$ cations.

Optical spectroscopy is a good method for probing the bandgaps of semiconductor materials through measurement of the absorbance and transmittance. The photographs in Fig. 7(a) show the 1D Magnéli-phase $Mo_4O_{11}$ nanorods grown on the ITO/glass substrates at temperatures of 1000, 1050, 1100, 1150, and 1200 ºC. It can be seen that all the 1D Magnéli-phase $Mo_4O_{11}$ nanorods grown on the ITO/glass substrates are blue. In fact, the nanorods synthesized at higher temperature are bluer. For example, the nanorods synthesized at 1000 ºC look light blue, while those synthesized at 1200 ºC become dark blue. Hence, one can expect to acquire a variety of absorbances and transmittances. The optical spectra in Figs. 7(b) and 7(c) show the absorbances and transmittances of 1D Magnéli-phase $Mo_4O_{11}$ nanorods synthesized at various temperatures, and are all different from each other in the range from ultraviolet (UV) to infrared (IR) lights. Obviously, the maximum transmittance for each spectrum appears at 422.1, 424.8, 428.3, 430.1, and 437.1 nm, and it is around 80, 52, 22, 11.5, and 2.5 % for the nanorods synthesized at 1000, 1050, 1100, 1150, and 1200 ºC, respectively. Similarly, the minimum absorbance for each

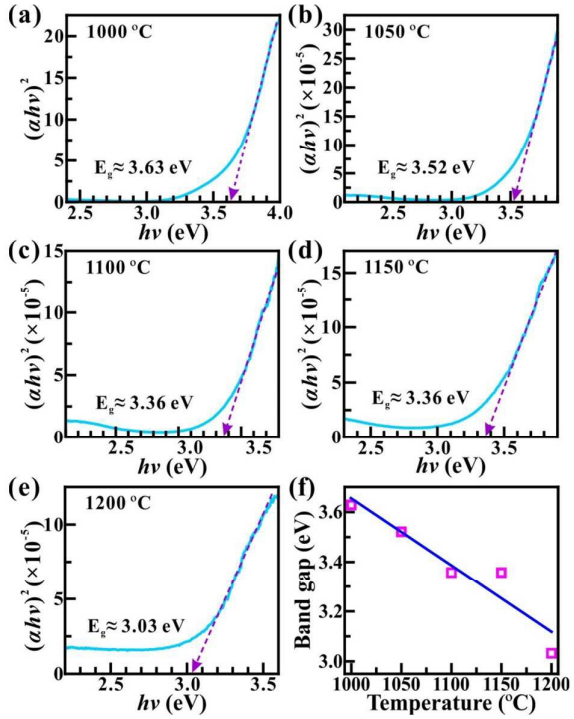


**Fig. 8** (a)-(e) Graphs of $(\alpha hv)^2$ versus $hv$ for determining the bandgaps ($E_g$) of the 1D $Mo_4O_{11}$ nanorods synthesized at 1000, 1050, 1100, 1150, and 1200 ºC. (f) The graph shows the bandgap ($E_g$) of the 1D Magnéli-phase $Mo_4O_{11}$ nanorods versus temperatures, and the bandgap is inversely proportional to the temperature.

spectrum occurs at 421.2, 421.7, 430.1, 430.1 and 436.7 nm, and they are about 0.1, 0.3, 0.7, 0.9 and 1.6 for the nanorods synthesized at 1000, 1050, 1100, 1150, and 1200 ºC, respectively. Hence, the graph in Fig. 7(d) shows the linear fit between two series of data for transmittance and absorbance *versus* temperatures. The shift of the transmittance maximum is inversely proportional to the temperature, but that of the absorbance minimum is linearly proportional to the temperature. These results indicate that the bandgaps ($E_g$) of 1D Magnéli-phase $Mo_4O_{11}$ nanorods are strongly and linearly dependent on the synthesis temperature.

The bandgaps ($E_g$) of the 1D Magnéli-phase $Mo_4O_{11}$ nanorods can be determined using the equation $\alpha hv = A(hv - E_g)^{1/2}$,[45] where $\alpha$ is absorption coefficiency and A is a constant. The absorbance spectra in Fig. 7(d) were converted to the graphs of $(\alpha hv)^2$ versus $hv$ in Fig. 8(a)-8(e) for determining the bandgaps ($E_g$) of the 1D Magnéli-phase $Mo_4O_{11}$ nanorods synthesized at 1000, 1050, 1100, 1150, and 1200 ºC, respectively. The straight lines are used to fit the edges of the converted curves. With regard to the extrapolation method, the fitting straight lines intersect at the $hv$ axes. The intersections can be determined as the values of the bandgaps ($E_g$), so the bandgaps ($E_g$) of the 1D Magnéli-phase $Mo_4O_{11}$ nanorods, synthesized at 1000, 1050, 1100, 1150, and 1200 ºC, are 3.63, 3.52, 3.36, 3.36, and 3.03 eV, respectively. The graph in Fig. 8(f) shows the bandgap ($E_g$) of the 1D Magnéli-phase $Mo_4O_{11}$ nanorods versus temperature. It is clear that the bandgap ($E_g$) decreases with elevation of the synthesis temperature, and there is a linear fit between the series of data for the bandgap versus temperature. Hence, the bandgap is inversely proportional to the temperature. As mentioned above, 1D Magnéli-phase $Mo_4O_{11}$ nanorods synthesized at various temperatures have varying combinations of two orthorhombic ($\alpha$) and monoclinic ($\eta$) phases, and mixtures of $Mo^{4+}$, $Mo^{5+}$ and $Mo^{6+}$ cations, which are suggested to be two main factors for tuning the bandgaps ($E_g$) of the 1D Magnéli-phase $Mo_4O_{11}$ nanorods without any doping. In other words, we can tune the bandgap ($E_g$) of the 1D Magnéli-phase $Mo_4O_{11}$ nanorods by controlling only the synthesis temperature. The results for bandgap tuning make the 1D Magnéli-phase $Mo_4O_{11}$ nanorods excellent for the fabrication of optoelectronic nanodevices to be used in bandgap engineering.

## Conclusions

We synthesized large-area arrays of 1D Magnéli phase $Mo_4O_{11}$ nanorods on ITO thin films coated on glass substrates using the HFMOVD technique at 1000, 1050, 1100, 1150, and 1200 °C. The widths of a large number of the 1D Magnéli-phase $Mo_4O_{11}$ nanorods fall into the range of ~20-60 nm. The 1D Magnéli-phase $Mo_4O_{11}$ nanorods comprise various combinations of the orthorhombic ($\alpha$) and monoclinic ($\eta$) phases, and varying mixtures of the $Mo^{4+}$, $Mo^{5+}$ and $Mo^{6+}$ cations at varying temperatures. The phase combination and cation mixture are the two main factors for tuning the bandgaps ($E_g$) of the 1D Magnéli-phase $Mo_4O_{11}$ nanorods without any doping. The bandgap ($E_g$) of the 1D Magnéli-phase $Mo_4O_{11}$ nanorods can be tuned by controlling only the synthesis temperature. Therefore, the 1D Magnéli-phase $Mo_4O_{11}$ nanorods are excellent materials for the fabrication of optoelectronic nanodevices in bandgap engineering.

## Acknowledgements

The authors would like to thank the Ministry of Science and Technology (MOST), Taiwan for their financial support of this research under Contract Nos. MOST-103-2112-M-259-006-MY2, MOST-103-2811-M-259-003, MOST-104-2811-M-259-008, MOST-102-2923-M-259-001-MY3, and MOST-102-2811-M-259-013.

## Notes and references

1 X. Y. Liu, C. X. Shan, H. Zhu, B. H. Li, M. M. Jiang, S. F. Yu, D.Z. Shen, *Ultraviolet lasers realized via electrostatic doping method*, Sci. Rep., 2015, **5**, 13641.
2 J. Sivasankari, S. Sankar, L. VimalaDevi, J. Mater. Sci: Mater. Electron., 2015, **26**, 8089-8096.
3 S. Maensiri, C. Masingboon, V. Promarak, S. Seraphin, Opt. Mater., 2007, **29**, 1700-1705.
4 G. M. Lohar, S. T. Jadhav, H. D. Dhaygude, M. V. Takale, R. A. Patil, Y.-R. Ma, M. C. Rath, V. J. Fulari, J. Alloy Compd., 2015, **653**, 22-31.

5 G. M. Lohar, H. D. Dhaygude, R. A. Patil, Y.-R. Ma, V. J. Fulari, J. Mater. Sci: Mater. Electron., 2015, **26**, 8904-8914.
6 G. M. Lohar, S. T. Jadhav, M. V. Takale, R. A. Patil, Y.-R. Ma, M. C. Rath, V. J. Fulari, J. Colloid Interface Sci., 2015, **458**, 136-146.
7 J.-B. Liu, P.-J. Li, Y.-F. Chen, Z.-G. Wang, F. Qi, J.-R. He, B.-J. Zheng, J.-H. Zhou, W.-L. Zhang, L. Gu, Y.-R. Li, Sci. Rep., 2015, **5**, 15285.
8 Y. L. Huang, Y. Chen, W. Zhang, S. Y. Quek, C.-H. Chen, L.-J. Li, W.-T. Hsu, W.-H. Chang, Y. J. Zheng, W. Chen, A. T. S. Wee, Nat. Comm., 2014, **6**, 6298.
9 R. S. Devan, R. A. Patil, J.-H. Lin, Y.-R. Ma, Adv. Funct. Mater., 2012, **22**, 3326-3370.
10 D. Liu, W. W. Lei, J. Hao, D. D. Liu, B. B. Liu, X. Wang, X. H. Chen, Q. L. Cui, G. T. Zou, J. Liu, S. Jiang, J. Appl. Phys., 2009, **105**, 023513.
11 R. Sivakumar, R. Gopalakrishnan, M. Jayachandran, C. Sanjeeviraja, Curr. Appl. Phys., 2007, **7**, 51-59.
12 V. Madhavi, P. Kondaiah, S. S. Rayudu, O. M. Hussain, S. Uthanna, Mater. Express, 2013, **3**, 135-143.
13 A. Arfaoui, B. Ouni, S. Touihri, A. Mhamdi, A. Labidi, T. Manoubi, Opt. Mater., 2015, **45**, 109-120.
14 G. Wei, W. Qin, D. Zhang, G. Wang, R. Kim, K. Zheng, L. Wang, J. Alloy. Compd., 2009, **481**, 417-421.
15 M. Dhanasankar, K. K. Purushothaman, G. Muralidharan, Solid State Sci., 2010, **12**, 246-251.
16 Y. Shen, R. Huang, Y. Cao, P. Wang, Mater. Sci. Eng. B, 2010, **172**, 237-241.
17 M. Davide, L. Henrik, B. Arumugam Chandra, O. Kostya, Nanotechnology, 2008, **19**, 495302.
18 W. Li, F. Cheng, Z. Tao, J. Chen, J. Phys. Chem. B, 2006, **110**, 119-124.
19 J. S. Chen, Y. L. Cheah, S. Madhavi, X. W. Lou, J. Phys. Chem. C, 2010, **114**, 8675-8678.
20 S. Balendhran, J. Deng, J. Z. Ou, S. Walia, J. Scott, J. Tang, K. L. Wang, M. R. Field, S. Russo, S. Zhuiykov, M. S. Strano, N. Medhekar, S. Sriram, M. Bhaskaran, K. Kalantar-zadeh, Adv. Mater., 2013, **25**, 109-114.
21 M. Shetty, K. Murugappan, T. Prasomsri, W. H. Green, Y. Román-Leshkov, J. Catal., 2015, **331**, 86-97.
22 A. Chithambararaj, N. S. Sanjini, S. Velmathi, A. C. Bose, Phys. Chem. Chem. Phys., 2013, **15**, 14761-14769.
23 Y. Chen, C. Lu, L. Xu, Y. Ma, W. Hou, J.-J. Zhu, CrystEngComm, 2010, **12**, 3740-3747.
24 D. Chen, M. Liu, L. Yin, T. Li, Z. Yang, X. Li, B. Fan, H. Wang, R. Zhang, Z. Li, H. Xu, H. Lu, D. Yang, J. Sun, L. Gao, J. Mater. Chem., 2011, **21**, 9332-9342.
25 N. Illyaskutty, H. Kohler, T. Trautmann, M. Schwotzer, V. P. M. Pillai, Sens. Actuator B-Chem., 2013, **187**, 611-621.
26 A. M. Taurino, A. Forleo, L. Francioso, P. Siciliano, M. Stalder, R. Nesper, Appl. Phys. Lett., 2006, **88**, 152111.
27 G. E. Buono-Core, A. H. Klahn, C. Castillo, E. Muñoz, C. Manzur, G. Cabello, B. Chornik, J. Non-Cryst. Solids, 2014, **387**, 21-27.
28 L. Kumari, Y.-R. Ma, C.-C. Tsai, Y.-W. Lin, S. Y. Wu, K.-W. Cheng, Y. Liou, X-ray diffraction and Raman scattering studies on large-area array and nanobranched structure of 1D $MoO_2$ nanorods, Nanotechnology, 2007, **18**, 115717.
29 A. Chithambararaj, B. Winston, N. S. Sanjini, S. Velmathi, A. C. Bose, J. Nanosci. Nanotechnol., 2015, **15**, 4913-4919.
30 M. Dieterle, G. Mestl, Phys. Chem. Chem. Phys., 2002, **4**, 822-826.
31 L. Kihlborg, A. Magnéli, Acta Chem. Scand., 1955, **9**, 471-474.
32 H. Werner, O. Timpe, D. Herein, Y. Uchida, N. Pfänder, U. Wild, R. Schlögl, H. Hibst, Catal. Lett., 1997, **44**, 153-163.
33 A. Magnéli, Acta Chem. Scand., 1948, **2**, 861-871.
34 M. Dieterle, G. Weinberg, G. Mestl, Phys. Chem. Chem. Phys., 2002, **4**, 812-821.
35 R. A. Patil, R. S. Devan, J.-H. Lin, Y. Liou, Y.-R. Ma, Sci. Rep., 2013, **3**, 3070.
36 J.-H. Lin, R. A. Patil, M.-A. Wu, L.-G. Yu, K.-D. Liu, W.-T. Gao, R. S. Devan, C.-H. Ho, Y. Liou, Y.-R. Ma, J. Mater. Chem. C, 2014, **2**, 8667-8672.
37 R. S. Devan, C.-L. Lin, J.-H. Lin, T.-K. Wen, R. A. Patil, Y.-R. Ma, J. Nanosci. Nanotechnol., 2013, **13**, 1001-1005.
38 R. A. Patil, R. S. Devan, J.-H. Lin, Y.-R. Ma, P. S. Patil, Y. Liou, Sol. Energy Mater. Sol. Cells, 2013, **112**, 91-96.
39 M. Borovsak, P. Sutar, E. Goreshnik, D. Mihailovic, Appl. Surf. Sci., 2015, **354**, 256-259.
40 M. E. Cura, X. W. Liu, U. Kanerva, S. Varjus, A. Kivioja, O. Söderberg, S.-P. Hannula, Tribol. Int., 2015, **87**, 23-31.
41 L. Wang, B. Li, *Phononics gets hot*, Phys. World, 2008, **21**, 27-29.
42 A. A. Balandin, D. L. Nika, Mater. Today, 2012, **15**, 266-275.
43 N. Li, J. Ren, L. Wang, G. Zhang, P. Haenggi, B. Li, Rev. Mod. Phys., 2012, **84**, 1045-1066.
44 M. Maldovan, Nature, 2013, **503**, 209-217.
45 N. Illyaskutty, S. Sreedhar, G. S. Kumar, H. Kohler, M. Schwotzer, C. Natzeck, V. P. M. Pillai, Nanoscale, 2014, **6,** 13882-13894.